

A Dense Current Flowing down a Sloping Bottom in a Rotating Fluid

C. CENEDESE AND J. A. WHITEHEAD

Woods Hole Oceanographic Institution, Woods Hole, Massachusetts

T. A. ASCARELLI

Universita' di Roma "La Sapienza," Rome, Italy

M. OHIWA

Woods Hole Oceanographic Institution, Woods Hole, Massachusetts

(Manuscript received 21 August 2002, in final form 15 July 2003)

ABSTRACT

A density-driven current was generated in the laboratory by releasing dense fluid over a sloping bottom in a rotating freshwater system. The behavior of the dense fluid descending the slope has been investigated by systematically varying four parameters: the rotation rate, the bottom slope, the flow rate of the dense fluid, and the density of the dense fluid. Over a wide range of parameter values, the following three flow types were found: a laminar regime in which the dense current had a constant thickness behind the head, a wave regime in which wavelike disturbances appeared on the interface between the dense and fresh fluids, and an eddy regime in which periodic formation of cyclonic eddies in the fresh overlying ambient fluid was observed. All of the experiments revealed that increasing the slope angle and the density of the bottom fluid allowed the flow to evolve from the laminar to the wave regime. Furthermore, increasing rotation rate induced the formation of eddies. A theoretical solution for the downslope velocity field has been found using a steady-state model. Comparison between the theoretical and experimental downslope velocities gave good agreement. The wave regime was observed to occur for values of the Froude number greater than 1. The laminar regime was found for values of the Froude number less than 1. The amount of mixing between the dense and the ambient fluids was measured. Mixing increased significantly when passing from the laminar to the wave regime, that is, with increasing Froude number. Good agreement between the amount of mixing observed in the ocean and in the laboratory experiments is encouraging and makes the waves observed in the present experiments a possible candidate for the mixing observed during oceanic dense current overflows.

1. Introduction

The descent of dense water from the continental shelves into the deep ocean over the continental slope is an important component of the thermohaline circulation. Sources of deep-water formation are found mainly in the polar regions (Warren 1981), and outflows to the main oceans are found in the Denmark Strait (Dickson and Brown 1994), in the Faroe Bank Channel (Saunders et al. 1990), on the Arctic continental shelves (Aagaard et al. 1981), and at various sites on the continental shelf of Antarctica in winter (Foster and Carmack 1976). There are also dense water currents from enclosed seas where evaporation contributes to increasing the density of the enclosed waters. These currents flow into the open seas through a strait, as in the case of the Mediterranean

outflow (Price et al. 1993). Consequently they descend the continental slope and enter the open ocean.

Furthermore, dense water descends downstream of gaps separating deep abyssal basins. Gaps with documented unidirectional flows of the densest water include the Ceara Abyssal Plain, the Vema Channel, Vema Gap, Discovery Gap, and the Romansch Fracture Zone (Whitehead 1998). In all cases, the dense water descends into the downstream basin and mixes with the surrounding water during its descent.

The dynamics of such dense currents on slopes have been modeled in the past both theoretically and experimentally starting with Ellison and Turner (1959) and Britter and Linden (1980), and a review on gravity currents can be found in Griffiths (1986). A review of existing observations of downslope flows around Antarctica together with possible dynamical mechanisms is presented by Baines and Condie (1998). In a simplified "streamtube" model (Smith 1975; Killworth 1977; Price and Barringer 1994), the dense plume flowed

Corresponding author address: Dr. Claudia Cenedese, Department of Physical Oceanography, Woods Hole Oceanographic Institution, MS #21, Woods Hole, MA 02543.
E-mail: ccenedese@whoi.edu

downslope balancing buoyancy, Coriolis and friction forces. This model considered the overlying ambient ocean at rest and averaged or ignored any three-dimensional effects so that the plume was not subject to any nonlinear instabilities. Price and Barringer (1994) included a Froude number parameterization of the entrainment and an Ekman number parameterization of the broadening. Strong mixing was found to be localized to regions with large bottom slope, typically the shelf-slope break, and a substantial entrainment of oceanic water was observed for the four major overflows analyzed in this study: the Mediterranean, the Denmark Strait, the Faroe Bank Channel outflows, and the Filchner ice shelf outflow into the Weddell Sea. This model considered a laterally integrated streamtube, while Jungclauss and Backhaus (1994) resolved the plume horizontally using a hydrostatic, reduced gravity, two-dimensional primitive equation numerical model. This latter study investigated the transient character of dense currents flowing down a slope and the effects of topographic disturbances. A model lying between the streamtube and the full three-dimensional models was developed by Shapiro and Hill (1997). Their $1\frac{1}{2}$ -layer theoretical model included bottom friction and entrainment and brought to light that a typical thickness of the plume is twice the bottom Ekman-layer scale, that vertical mixing enhances downslope propagation of the dense current, and that an interior current can either enhance or oppose the dense current descent. Recently, numerical models have included the dynamic interaction of the dense flow with the ambient fluid above (Chapman and Gawarkiewicz 1995; Jiang and Garwood 1995, 1996, 1998; Spall and Price 1998; Swaters 1998) and have shown that a strong coupling between the two layers can lead to the formation of cyclonic vortices. Similar vortex formation was observed near the Denmark Strait (Bruce 1995; Krauss 1996) and in earlier laboratory experiments (Whitehead et al. 1990). The eddies can be generated by either a process in which the upper-layer columns get stretched, conserving potential vorticity (Lane-Serff and Baines 1998, 2000; Etling et al. 2000), or by baroclinic instability (Smith 1977; Etling et al. 2000; Morel and McWilliams 2001). Once formed, these eddies move across slope as described by Mory et al. (1987). However, the descent of dense water down a slope is not always associated with eddy formation. Shapiro and Zatsepin (1996) and Zatsepin et al. (1996) observed the interface above a dense bottom current to become unstable to growing waves, and a linear stability analysis showed that the stability threshold depended on the Froude number. Nagata et al. (1993) compared the downslope velocity component of a dense current with a theoretical estimate based on a steady-state model that is valid for small slope angles. The agreement was good for low values of the Coriolis parameter, while for large values, the magnitude of the experimental speeds was larger than the theoretical estimates. Last, a recent study by Ozgokmen and Chas-

signet (2002) investigated the mechanism of mixing in a nonrotating gravity current descending a slope using a two-dimensional, nonhydrostatic, numerical model with a high horizontal and vertical resolution that permitted the capture of the Kelvin–Helmholtz instability in the head and trailing fluid of the gravity current. The turbulent entrainment of ambient fluid associated with this instability is found to be stronger than the laminar entrainment related to the head growth caused by the drag exerted by the fresh fluid in front. Entrainment into a turbulent jet descending into a rotating stratified reservoir has been investigated also in the laboratory by Davies et al. (2002) and resulted in the formation of an intermediate density boundary current.

The purpose of this paper is to investigate, over a wide range of parameters, the behavior of a dense current flowing down a slope and to quantitatively identify the transition between the three main regimes observed separately in the past: the laminar, the wave, and the eddy regime. Although each of these regimes have been previously discussed in different studies, a comprehensive study of all of the regimes showing the fundamental parameters that define each regime is still lacking. In section 2, we develop a steady-state model similar to Nagata et al. (1993), but valid for any slope angles. Our model is a simplified version of the Shapiro and Hill (1997) model but it allows us to find analytical solutions for the downslope velocity of the dense current while the advection–diffusion type of governing equation of the Shapiro and Hill (1997) model allows estimates of the velocity, but the full solution can only be found numerically. The predicted velocities found with our model are in good agreement with the experimental velocities measured in both the laminar and wave regime. The experimental apparatus is described in section 3. In section 4 we describe the behavior of the dense current for the nonrotating experiments, while the rotating experiments are discussed in sections 5 and 6. In section 7, we investigate the influence of the observed growing waves on the mixing between the two layers and compare the mixing to the values measured in the ocean and in previous laboratory experiments in section 8. The conclusions of the work are also discussed in section 8.

2. Theoretical model

The purpose of this model is to provide a solution for a laminar flow descending a sloping bottom.

a. Formulation of the model

We seek a solution for steady flow of a dense layer of constant thickness over a sloping bottom. We consider two fluids of constant uniform densities ρ_1 and ρ_2 , with $\rho_2 > \rho_1$ as shown in Fig. 1. Both fluids have kinematic viscosity ν . The bottom layer has constant thickness so the interface is parallel to the sloping bottom with slope $s = \tan\theta$, where θ is the angle between

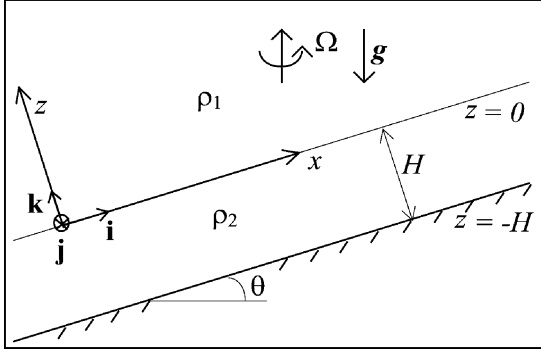


FIG. 1. Sketch of the model configuration.

the slope and the horizontal. The upper fluid is considered to be infinitely deep. The fluids are in a frame rotating with angular velocity Ω , parallel to gravity. The Coriolis parameter is $f = 2\Omega$. The centrifugal force is neglected, and we subtract the hydrostatic pressure distribution within the upper fluid. In the rotating frame of reference, we adopt the tilted coordinates \mathbf{i} (directed up the slope), \mathbf{j} (directed across slope, the left looking up the slope being positive), and \mathbf{k} (directed upward normal to the bottom) shown in Fig. 1. The rigid sloping bottom is defined by the boundary $z = -H$, where H is the depth of the lower layer, while the interface is defined by the surface $z = 0$. The velocity has components $u_n, v_n, w_n, n = 1, 2$, parallel to the tilted x, y, z axes, respectively.

We seek fully developed flow parallel to the sloping bottom and thus set $w_n = 0$. The linearized, steady Boussinesq momentum equations in the upper fluid obey

$$-(2\Omega \cos\theta)v_1 = \nu \frac{\partial^2 u_1}{\partial z^2} \quad \text{and} \quad (1)$$

$$(2\Omega \cos\theta)u_1 = \nu \frac{\partial^2 v_1}{\partial z^2}. \quad (2)$$

The lower layer obeys

$$-(2\Omega \cos\theta)v_2 = \nu \frac{\partial^2 u_2}{\partial z^2} - g \frac{(\rho_2 - \rho_1)}{\rho_1} \sin\theta \quad \text{and} \quad (3)$$

$$(2\Omega \cos\theta)u_2 = \nu \frac{\partial^2 v_2}{\partial z^2}. \quad (4)$$

The last term on the right-hand side of (3) represents the buoyancy forcing of the system due to the dense fluid layer on the slope. Equations (1) and (2) are the standard Ekman layer equations having solution

$$v_1 = A \sin(z/\delta)e^{-z/\delta} + B \cos(z/\delta)e^{-z/\delta} \quad \text{and} \quad (5)$$

$$u_1 = -A \cos(z/\delta)e^{-z/\delta} + B \sin(z/\delta)e^{-z/\delta}, \quad (6)$$

where $\delta = \sqrt{2\nu/f_*}$ is the Ekman layer depth, $f_* = 2\Omega \cos\theta$, and A and B are constants. Similarly in the lower layer the solution takes the form

$$v_2 = C \sin(z/\delta)e^{-z/\delta} + D \cos(z/\delta)e^{-z/\delta} + E \sin(z/\delta)e^{z/\delta} + F \cos(z/\delta)e^{z/\delta} + v_p \quad \text{and} \quad (7)$$

$$u_2 = -C \cos(z/\delta)e^{-z/\delta} + D \sin(z/\delta)e^{-z/\delta} + E \cos(z/\delta)e^{z/\delta} - F \sin(z/\delta)e^{z/\delta}, \quad (8)$$

where

$$v_p = \frac{1}{2\Omega} g \frac{(\rho_2 - \rho_1)}{\rho_1} \frac{\sin\theta}{\cos\theta} \quad (9)$$

is the particular solution of (3) and C, D, E, F are constants. Equation (9) is the across-slope velocity for a geostrophic flow (neglecting friction) and it is also the long Rossby wave speed (Nof 1983).

b. Solutions

The values of the constants in these solutions depend on the boundary conditions. Let us consider a nonslip bottom boundary condition, $v_2 = 0$ and $u_2 = 0$ for $z = -H$, and set the velocity and the stress to be continuous on the interface between the two layers, $v_1 = v_2, u_1 = u_2, \partial v_1/\partial z = \partial v_2/\partial z$, and $\partial u_1/\partial z = \partial u_2/\partial z$ at $z = 0$.

These conditions produce

$$A = C = v_p J, \quad B = D - F, \\ D = v_p K, \quad E = 0, \quad \text{and} \quad F = -\frac{1}{2}v_p, \quad (10)$$

where

$$J = -\sin\left(\frac{2H}{\delta}\right) \frac{e^{-2H/\delta}}{2} + \sin(H/\delta)e^{-H/\delta} \quad \text{and}$$

$$K = \cos\left(\frac{2H}{\delta}\right) \frac{e^{-2H/\delta}}{2} - \cos(H/\delta)e^{-H/\delta}.$$

The full solution is

$$u_1 = v_p \left(-J \cos\frac{z}{\delta} e^{-z/\delta} + K \sin\frac{z}{\delta} e^{-z/\delta} + \frac{1}{2} \sin\frac{z}{\delta} e^{-z/\delta} \right), \quad (11)$$

$$v_1 = v_p \left(J \sin\frac{z}{\delta} e^{-z/\delta} + K \cos\frac{z}{\delta} e^{-z/\delta} + \frac{1}{2} \cos\frac{z}{\delta} e^{-z/\delta} \right), \quad (12)$$

$$u_2 = v_p \left(-J \cos\frac{z}{\delta} e^{-z/\delta} + K \sin\frac{z}{\delta} e^{-z/\delta} + \frac{1}{2} \sin\frac{z}{\delta} e^{z/\delta} \right), \quad (13)$$

and

$$v_2 = v_p \left(J \sin\frac{z}{\delta} e^{-z/\delta} + K \cos\frac{z}{\delta} e^{-z/\delta} - \frac{1}{2} \cos\frac{z}{\delta} e^{z/\delta} + 1 \right). \quad (14)$$

The flux in the top fluid in the across-slope direction is

$$u_{1F} = \int_0^\infty u_1 dz = \frac{\delta v_p}{2} \left(-J + K + \frac{1}{2} \right), \quad (15)$$

and the across-slope bottom layer flux is

$$\begin{aligned} u_{2F} &= \int_{-H}^0 u_2 dz \\ &= \frac{\delta v_p}{2} \left[(-J + K) \cos \frac{H}{\delta} e^{H/\delta} - (J + K) \sin \frac{H}{\delta} e^{H/\delta} \right. \\ &\quad \left. + \frac{1}{2} \left(\sin \frac{H}{\delta} + \cos \frac{H}{\delta} \right) e^{-H/\delta} + J - K - \frac{1}{2} \right]. \end{aligned} \quad (16)$$

The flux in the top fluid in the downslope direction is

$$v_{1F} = \int_0^\infty v_1 dz = \frac{\delta v_p}{2} \left(J + K + \frac{1}{2} \right), \quad (17)$$

and in the bottom layer it is

$$\begin{aligned} v_{2F} &= \int_{-H}^0 v_2 dz \\ &= \frac{\delta v_p}{2} \left[(J + K) \cos \frac{H}{\delta} e^{H/\delta} - (J - K) \sin \frac{H}{\delta} e^{H/\delta} \right. \\ &\quad \left. + \frac{1}{2} \left(\cos \frac{H}{\delta} - \sin \frac{H}{\delta} \right) e^{-H/\delta} - J - K - \frac{1}{2} \right] \\ &\quad + v_p H. \end{aligned} \quad (18)$$

We will discuss two limits obtained for large and small Ekman numbers, $\text{Ek} = (\delta/H)^2$. It is useful to inspect the solution for $\text{Ek} \ll 1$ by setting $H/\delta \gg 1$. In that case there are Ekman layers. We set $J = K = O(e^{-H/\delta})$, which is small; consequently, the fluxes to first order are

$$u_{1F} = v_{1F} = \frac{\delta v_p}{4} \quad \text{and} \quad (19)$$

$$u_{2F} = -3u_{1F}, \quad v_{2F} = v_p H + u_{2F}. \quad (20)$$

The effective volume flux thickness is $\delta/4$. Fluid moves up the slope by Ekman pumping in the top fluid and three times more fluid moves down the slope in the bottom layer. Fluid in the bottom layer moves across the slope in thermal wind balance with an additional flux in the boundary layers, and the top fluid flux is found in a boundary layer moving across the slope in the same direction as the thermal wind flow. Since $H \gg (\delta/4)$ the thermal wind flux $v_p H$ across the slope is larger than the flux in the boundary layers as also found by Shapiro and Hill (1997). Typical flows are shown for H/δ large but close to 1 ($\text{Ek} = 0.043$) in Fig. 2a and for larger H/δ ($\text{Ek} = 0.01$) in Fig. 2b.

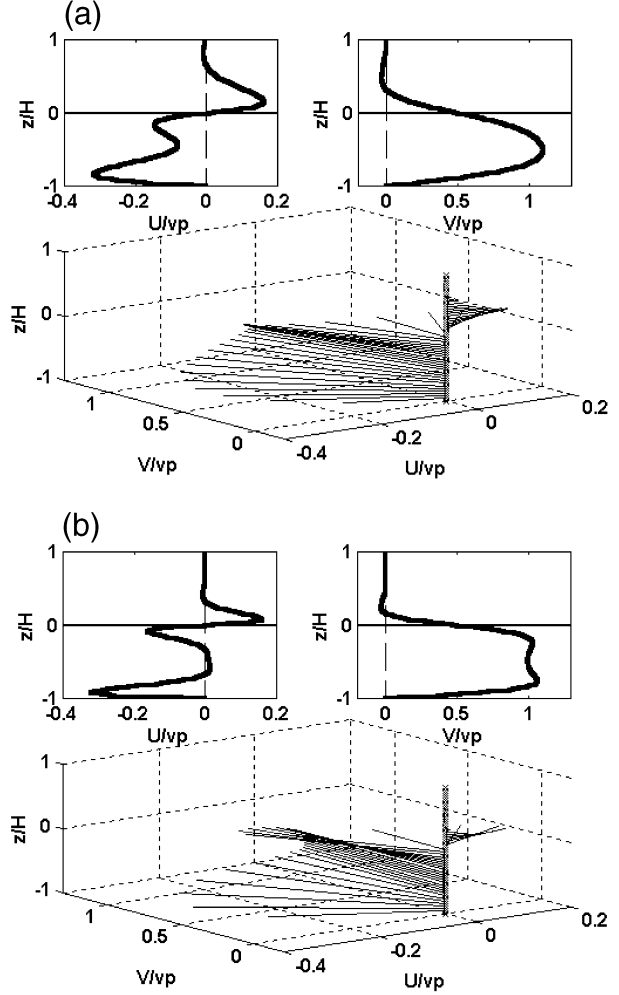


FIG. 2. Nondimensional velocity section in (top left) the x - z plane and (top right) the y - z plane and (bottom) 3D velocity vectors (a) for values of the Ekman number $\text{Ek} = 0.043$ and the Ekman layer depth $\delta = 0.10$ cm ($f = 2$ s $^{-1}$, $H = 0.5$ cm, $g' = 2.0$ cm s $^{-2}$, and $s = 0.4$). (b) As in (a) but for values of the Ekman number $\text{Ek} = 0.01$ and the Ekman layer depth $\delta = 0.05$ cm ($f = 8.0$ s $^{-1}$, $H = 0.5$ cm, $g' = 2.0$ cm s $^{-2}$, and $s = 0.4$). The x , y , and z axes correspond to the tilted coordinate system shown in Fig. 1.

The other limit is for large Ek for which we expand the variables as a power series in z/δ for $H/\delta \ll 1$. The velocity in the top fluid is

$$u_1 = -v_v \left[\left(1 - \frac{H}{\delta} \right) \cos \frac{z}{\delta} - \frac{H}{\delta} \sin \frac{z}{\delta} \right] e^{-z/\delta}, \quad \text{and} \quad (21)$$

$$v_1 = v_v \left[\left(1 - \frac{H}{\delta} \right) \sin \frac{z}{\delta} + \frac{H}{\delta} \cos \frac{z}{\delta} \right] e^{-z/\delta}, \quad (22)$$

where $v_v = v_p (H/\delta)^2$ is the Stokes flow velocity for a layer of viscous fluid traveling down the slope [see Eq. (6–18) in Schubert and Turcotte (2002)]. The flux in the top fluid is

$$v_{1F} = -u_{1F} = \frac{\delta v_v}{2}. \quad (23)$$

A large volume flux is dragged toward a deeper region, and this fluid also moves across the slope in the direction of a current driven by thermal wind. The velocity in the bottom layer is

$$u_2 = -v_v \left(1 - \frac{z^2}{H^2} \right) \quad \text{and} \quad (24)$$

$$v_2 = \frac{1}{\delta} v_v (z + H). \quad (25)$$

The former is the simple viscous flow down a slope. The latter is smaller than the former, as also found in Shapiro and Hill (1997), and is not usually included in studies of geophysical gravity currents where planetary rotation is completely neglected. However, since $\delta \gg H$ in this limit, the flux of the top fluid (23) is greatest of all and rotation produces an important effect that is usually neglected. Figure 3 shows such flows for two cases with $H/\delta = 1.5$ ($\text{Ek} = 0.43$) and $H/\delta = 0.3$ ($\text{Ek} = 10.8$). The flux in the bottom layer is

$$u_{2F} = -\frac{2}{3} v_v H \quad \text{and} \quad v_{2F} = \frac{1}{2} v_v \frac{H^2}{\delta}.$$

These solutions will be used to determine some of the properties of the experimental runs.

3. Experimental apparatus

The experiments were conducted in a glass tank of depth 60 cm and length and width of 61 cm. This was mounted concentrically on a 1-m-diameter rotating turntable with a vertical axis of rotation. We used a square tank to avoid optical distortion from side views associated with a circular tank. A sketch of the apparatus is shown in Fig. 4. The tank had a bottom slope, $s = \tan\theta$, where θ is the angle between the slope and the horizontal, and it was filled with freshwater of density ρ_1 , which was initially in solid body rotation. A reservoir (B) of salted and dyed water of density $\rho_2 > \rho_1$ was placed on the rotating table and connected to a nozzle via a submersible pump and a plastic tube. A flowmeter (C) was positioned between the reservoir and the nozzle together with a valve (D) for flow rate regulation. The nozzle was covered with sponge in order to reduce mixing near the source between the dense fluid and the fresh ambient water, and it was positioned on the right side (looking upslope) of the shallowest part of the tank about 1–2 cm from the bottom.

Over 300 runs were conducted. For each rotating experiment, the ambient fluid was spun up for as long as 5 times the Ekman spinup time. The experiment commenced by switching on the submersible pump; at this time the video camera (E) was turned on. A current was established during each experiment, at the end of which

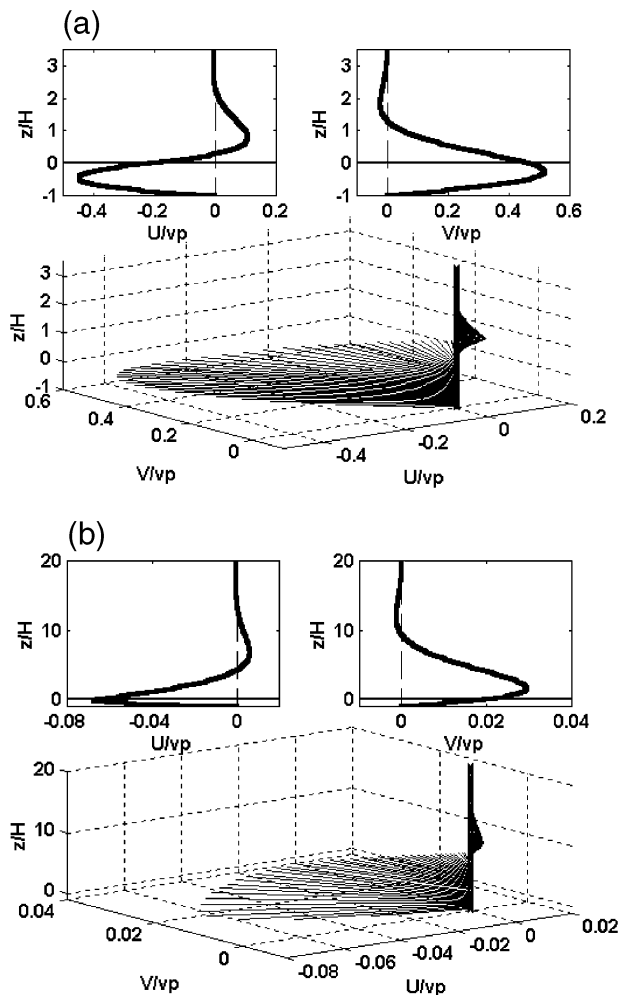


FIG. 3. Nondimensional velocity section in (top left) the x - z plane and (top right) the y - z plane and (bottom) 3D velocity vectors (a) for values of the Ekman number $\text{Ek} = 0.43$ and the Ekman layer depth $\delta = 0.33$ cm ($f = 0.2$ s $^{-1}$, $H = 0.5$ cm, $g' = 2.0$ cm s $^{-2}$, and $s = 0.4$). (b) As in (a) but for values of the Ekman number $\text{Ek} = 10.8$ and the Ekman layer depth $\delta = 1.6$ cm ($f = 0.008$ s $^{-1}$, $H = 0.5$ cm, $g' = 2.0$ cm s $^{-2}$, and $s = 0.4$). The x , y , and z axes correspond to the tilted coordinate system shown in Fig. 1.

the water in the tank was mixed and a new ambient density was measured for the following experiment. Two modifications were made to the apparatus described above when we conducted a set of experiments aimed at measuring the mixing between the dense current and the overlying fresh ambient water (see section 7). The first modification was made to reduce the mixing at the nozzle. We eliminated the nozzle, and roughly in the same location we positioned, on the sloping bottom, a plastic square box (10×10 cm) 5 mm in height, with the wall looking downslope removed. The tube from the pump was connected to an opening made on the top of this plastic box, and the dense water filled the box thickness and then exited the box on the downslope side (see Fig. 4, insert ii). The second modification was made

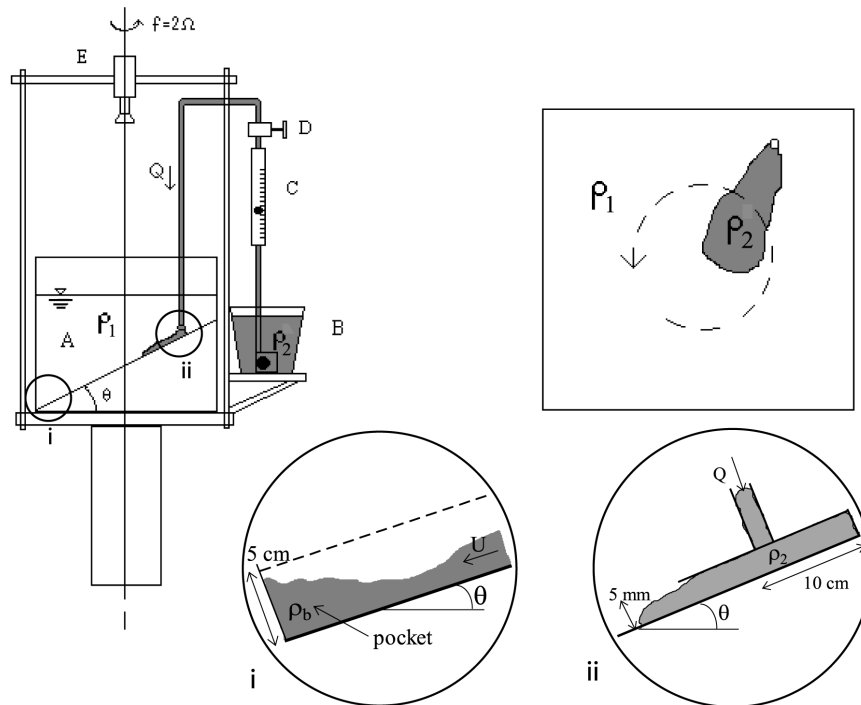


FIG. 4. Sketch of the experimental apparatus. (left) Side view and (right) plan view of the tank: (A) freshwater tank, (B) dense water reservoir, (C) flowmeter, (D) regulation valve for the dense flow, and (E) the video camera; ρ_1 and ρ_2 are the density of the freshwater and dense water, respectively. The dashed circle and arrowhead indicate the rotation direction. Inserts (i) and (ii) show details of the modifications made for the experiments described in section 7; ρ_b is the density of the current after it descended the slope.

to collect the dense water at the bottom of the slope without introducing further mixing. A 5-cm-high wall was attached orthogonal to the bottom and sides (dashed line in Fig. 4, insert i) of the slope, creating a pocket at the bottom of the slope where we collected samples of the dense water after it descended downslope (see Fig. 4, insert i). Samples were collected while the experiment was still rotating by means of a small diameter tube placed in the bottom of the pocket. As discussed in section 6, we presume that the mixing was caused by highly nonlinear waves with such high amplitudes that the thickness of the dense fluid in the wave trough is less than a millimeter. Hence, the mixing induced by the waves is believed to affect the entire fluid within the density current. Therefore, the fluid in the pocket at the bottom of the slope is presumed to be of uniform density; that is, the lower dense layer is well mixed.

The video camera (E) was mounted above the tank and fixed to the turntable so that measurements could be obtained in the rotating frame. The dense current was made visible by dyeing the fluid with food coloring and was observed both from the top and side view. The flow at the free surface was observed by adding buoyant paper pellets. The depth of the freshwater on the shallowest side of the tank was kept constant at 10 cm for every slope inclination and the following values of the Coriolis parameter f were used: 0.0, 0.2, 0.5, 0.7, 1.0,

1.2, 1.5, 1.7, 2.0, and 2.2 s^{-1} . For most of the experiments, the bottom slope $s = \tan\theta$ took the values of: 0.1, 0.25, 0.3, 0.4, 0.5, 0.6, and 0.7. However, in the experiments that measured mixing (see section 7), 18 values of the slope s within the same range (0.1 to 0.7) were used. The dense fluid was pumped in at a flow rate Q that ranged between 0.45 and $41.60 \text{ cm}^3 \text{ s}^{-1}$. Typically, about six values of Q were used with each values of f , s , and g' . The nozzle inner radius was kept constant at 0.3 cm. The buoyancy forces are described by the reduced gravity $g' = g(\rho_2 - \rho_1)/\rho_1$, where g is the gravitational acceleration, and g' took the values: 2, 4, 10, and 20 cm s^{-2} . The densities were determined with a model DMA58 Anton Paar densitometer with an accuracy of $10^{-5} \text{ g cm}^{-3}$. The thickness of the dense current, H , was measured by eye, with an error of approximately $\pm 2 \text{ mm}$, looking at the side view of the tank where a ruler, attached to the side wall, was placed orthogonal to the sloping bottom.

The velocity of the dense current, defined as the velocity of the current head or of the wave crests (see below), was measured by digitizing images of the experiment from the video tape at fixed time intervals and by selecting, on those images, a rectangular area where the dense fluid was present. The dye in the dense fluid made regions with higher thickness (like the head of the dense current or the crests of wavy interfacial pertur-

bations) have darker intensities than regions with lower thickness (like the trough of wavy interfacial perturbations). We then calculated the values of the cross-correlation function, C_n , between an image at an initial time t_0 and an image at time t_1, t_2, \dots, t_n , respectively. The distance between the origin and the maximum of the cross-correlation function, C_n , was the average displacement of the current head or of the wave crests in the time interval $(t_n - t_0)$, and from the displacement and the time interval we obtained the velocity and the angle of propagation of either the current head or of the wave crests in each time interval. We defined the velocity and the angle of propagation in each experiment by the mean of these values. Furthermore, we obtained the value of the wavelength and, again, the direction of propagation of the waves by computing the autocorrelation function, A_0 , of one image. The distance between the origin and the maximum of the autocorrelation function was the average wavelength and indicated the angle of propagation of the wave crests in the image considered.

4. Nonrotating experiments

All the experiments described hereafter are constant flux experiments in which fluid of density ρ_2 was added continuously from a small source positioned near the bottom. After the dense water was released at the nozzle on the right side (looking upslope) of the shallowest part of the tank, it started flowing downslope. The leading part of the front formed a “head” that was thicker than the fluid behind and had the characteristics described by Simpson (1997) with a region, behind the head, where some mixing occurred. The amount of mixing related to the head of the current depends on the Reynolds number (Simpson 1997; Schmidt 1911). For low Reynolds number, viscous forces predominate over buoyancy forces and very little mixing is apparent. As the Reynolds number increases, the buoyancy forces prevail on the viscous forces and eventually, for $Re > 1000$, eddies can be seen streaming back from the head. In the experiments described in this paper $Re = UH/\nu < 300$, hence the mixing associated with the head of the current was very small. The width of the current grew as it flowed down the slope and, for $f = 0 \text{ s}^{-1}$, it reached an approximately constant value some distance downstream. For the experiment with $f = 0 \text{ s}^{-1}$, the dense current descended exclusively downslope (with no across-slope flow). Over the range of parameter values investigated, two flow types were found: laminar flow and waves.

a. Laminar flow

In some cases, after leaving the source region the dense fluid behind the head had a constant thickness and a very sharp interface with the freshwater layer, indicating that no mixing was occurring between the

two fluids. From the side view, we observed that the raised head was a zone of “backward breaking” waves, but the viscous forces dominated over the buoyancy forces and the head was very small. The head was not observed to grow in size, and very little mixing occurred behind it (see section 7).

b. Waves

A wavelike disturbance on the interface between the dense and fresh fluids was observed in the plane orthogonal to the bottom slope. These disturbances, analogous to those previously observed by Alavian and Asce (1986), were parabolic in plane view and traveled downslope slightly faster than the head of the current. A detailed description of the waves is presented for the rotation experiments in the next section.

In these experiments the bottom slope was held constant at $s = 0.30$ and only the flow rate Q and the reduced gravity g' were varied. For values of $g' = 2 \text{ cm s}^{-2}$ waves were not observed and the dense current descended the slope in a laminar fashion. The waves appeared to grow on the interface between the two fluids for all values of $Q \geq 4 \text{ cm}^3 \text{ s}^{-1}$ and $g' = 10 \text{ cm s}^{-2}$. For $g' = 20 \text{ cm s}^{-2}$, waves appeared to grow for all values of Q . We expect that increasing the slope with a fixed value of $g' = 2 \text{ cm s}^{-2}$ would have given similar results because, as the slope increases, the waves would have been generated within the dense current. As expected, eddies were never observed in the nonrotating experiments.

5. Rotating experiments: Qualitative results

When $f > 0 \text{ s}^{-1}$, the current was influenced by rotation and its flow had an across-slope component. The dense current initially moved downslope for a length scale approximately equal to the Rossby radius of deformation, $R_D = \sqrt{g'H/f}$. This motion was deflected leftward (looking upslope) by the effect of rotation until the current reached a steady state in which the Coriolis force associated with the across-slope velocity balanced the viscous force and the downslope pressure force associated with the dense current. This transient regime took place over a time scale on the order of one inertial period. We systematically varied the slope s , the Coriolis parameter f , the reduced gravity g' , and the flow rate Q in order to observe their influence on the flow behavior. Over the range of parameter values investigated, three flow types were found: laminar flow, waves, and eddies.

a. Laminar flow

This regime has been described in the previous section and the effect of rotation caused the flow to veer to the left when looking upslope as shown in Fig. 5.

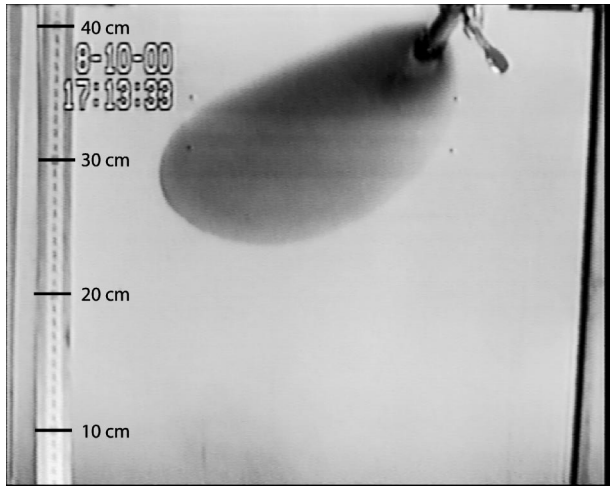


FIG. 5. Top view of the laminar flow observed after 3.8 revolutions for $f = 0.7 \text{ s}^{-1}$, $Q = 2.5 \text{ cm}^3 \text{ s}^{-1}$, $s = 0.3$, and $g' = 2 \text{ cm s}^{-2}$. A correction factor of 1.5 must be applied to the scale on the left side of the figure because the ruler was positioned on the top of the tank instead of at the level of the dense current.

Other than this aspect, the behavior of the current was similar to the nonrotating current.

b. Waves

For some experiments, the dense fluid flowed downslope, exhibited a “laminar flow” region (see top part of Fig. 6), and then started developing wavelike disturbances on the interface between the dense and fresh fluids. In the plane parallel to the sloping bottom the waves had a parabolic front. The wave crests are visible in the middle and bottom part of Fig. 6 as the regions of darker intensity. The crests traveled downslope in the same direction as, and slightly faster than, the head of the current. However, it was not possible to discern a

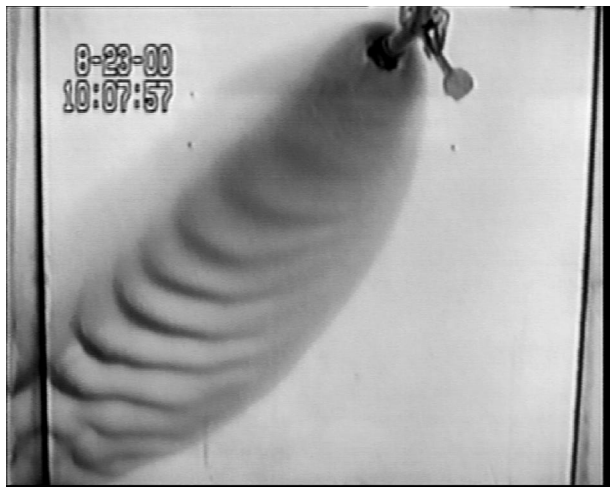


FIG. 6. Top view of the wave regime observed after 3.1 revolutions for $Q = 5 \text{ cm}^3 \text{ s}^{-1}$, $f = 0.7 \text{ s}^{-1}$, $s = 0.3$, and $g' = 10 \text{ cm s}^{-2}$.

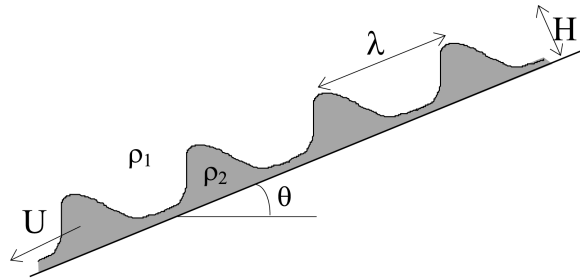


FIG. 7. Sketch of the waves moving downslope.

growth in size of the head of the current, possibly because the width of the waves (almost the same as the width of the current) increased while flowing downslope (see Fig. 6), hence redistributing the dense fluid over a larger area.

We allowed some experiments to run sufficiently long for the head of the current to reach the bottom of the tank. This did not affect the nature of the upstream gravity current. Hence, we do not focus on resolving the details at the gravity current head, which we consider to be part of a transition stage that lasts until the current head reaches the bottom of the slope and the waves are well established along the gravity current covering the whole length of the slope. In the plane orthogonal to the bottom slope, the dense current had a wave profile with alternating regions in which the bottom layer was thick (crests) and thin (troughs) as shown schematically on Fig. 7. The wave amplitude grew as each crest traveled downslope and the classic “backward breaking” crests were observed in most of the experiments (Fig. 8). We presume that mixing between the dense salty water and the lighter freshwater occurred. Furthermore, for some parameter values, the waves grew to such large amplitudes that they were observed to break in a three-dimensional fashion, giving the dense current a more

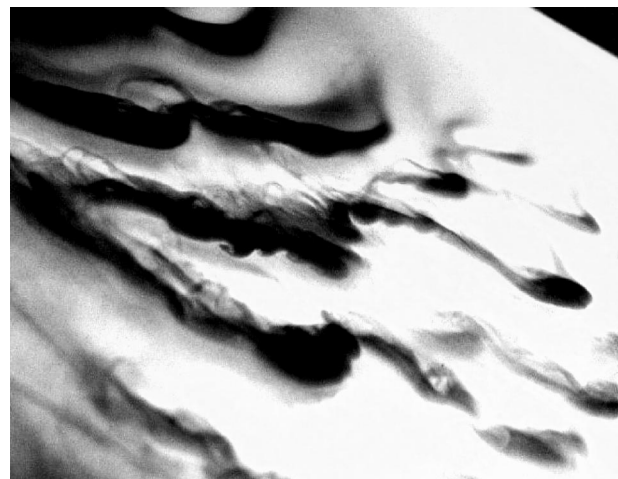


FIG. 8. Picture showing the three-dimensional waves. The “backward breaking” of the wave crests is also visible, as indicated by the lighter gray regions.

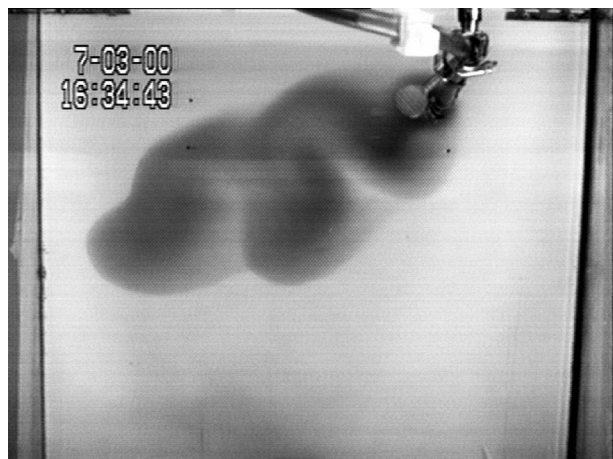


FIG. 9. Top view of the eddies observed after 23.3 revolutions for $Q = 1.45 \text{ cm}^3 \text{ s}^{-1}$, $f = 1.8 \text{ s}^{-1}$, $s = 0.25$, and $g' = 2 \text{ cm s}^{-2}$.

turbulent appearance (Fig. 8). The influence of wave breaking on the amount of mixing between the two water masses has been investigated for some of these experiments as discussed in section 7.

c. Eddies

In some experiments, the downslope movement of the dense fluid caused the periodic formation of cyclonic eddies in the freshwater above the dense fluid (Fig. 9). A possible mechanism for eddy generation is as follows: when dense water was introduced by the source near the bottom, the upper-layer thickness decreased from a depth h_0 to a depth $h_0 - h_c$, where h_0 is the ambient fluid depth at the source before the dense fluid is introduced in the tank and h_c is the dense current depth at the source. In order to conserve potential vorticity, the upper layers acquired a vorticity ζ given by

$$\frac{f}{h_0} = \frac{f + \zeta}{h_0 - h_c}. \quad (26)$$

Hence $\zeta = -fh_c/h_0$ and the upper layer started spinning anticyclonically capturing the dense fluid below. The dense fluid then coupled with the layer above and carried the anticyclonic column of freshwater above it downslope; consequently, the vorticity in the upper layer changed sign due to vortex stretching and potential vorticity conservation, and the freshwater column started spinning cyclonically. Similar behavior has been found previously, as discussed by Whitehead et al. (1990), Lane-Serff and Baines (1998, 2000), Spall and Price (1998), and Etling et al. (2000). The cyclonic eddies in the freshwater column were observed to move zonally leftward (looking upslope) until they reached the wall of the tank (Fig. 9) and they caused the lower dense layer to acquire a dome shape under each eddy with a height larger than the dense current thickness.

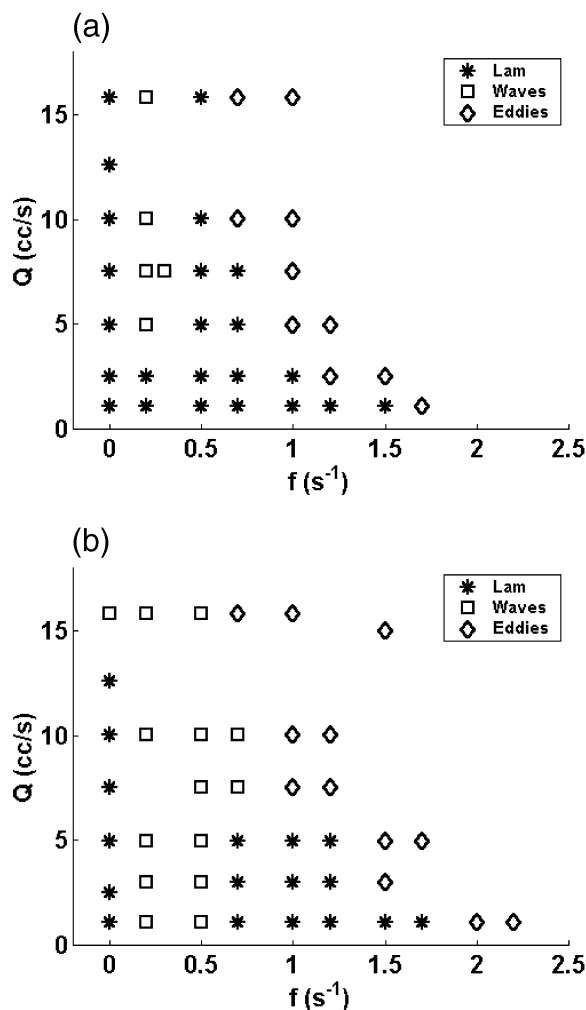


FIG. 10. Diagram showing the distribution of the three regimes for two sets of experiments with $g' = 2 \text{ cm s}^{-2}$ and (a) $s = 0.3$ and (b) $s = 0.4$. The other four diagrams discussed in section 6 are not shown.

6. Rotating experiments: Quantitative results

The three regimes described in section 5 occurred for different values of the parameters s , g' , f , and Q . Figure 10 illustrates the experiments for a fixed value of $g' = 2 \text{ cm s}^{-2}$ and two different slopes, $s = 0.3$ and $s = 0.4$. For the low value of the bottom slope $s = 0.25$ and the lowest value of $g' = 2 \text{ cm s}^{-2}$ (not shown), the wave regime was not observed and the passage from the laminar regime to the eddy regime occurred while increasing f . For flow rates in the range $0.45 \leq Q < 6.00 \text{ cm}^3 \text{ s}^{-1}$, the transition between the two regimes was found for $0.7 \leq f \leq 1.5 \text{ s}^{-1}$, while for $6.00 \leq Q \leq 18 \text{ cm}^3 \text{ s}^{-1}$, the transition occurred for $0.5 \leq f \leq 0.7 \text{ s}^{-1}$.

For all other parameter values, the wave regime was observed. While keeping the reduced gravity fixed at $g' = 2 \text{ cm s}^{-1}$ (Fig. 10) and increasing the bottom slope from $s = 0.30$ to $s = 0.50$, the wave regime first occurred for the lowest values of f (approximately $0 < f \leq 0.3 \text{ s}^{-1}$) and $Q \geq 4 \text{ cm}^3 \text{ s}^{-1}$; while for the highest

value of $s = 0.5$ (not shown) it was observed for approximately $f \leq 1.3 \text{ s}^{-1}$ for $Q \leq 10 \text{ cm}^3 \text{ s}^{-1}$ and for $f \leq 1.0 \text{ s}^{-1}$ for $Q \leq 15 \text{ cm}^3 \text{ s}^{-1}$. For a slope $s = 0.30$, the transition between the laminar regime and the eddy regime (Fig. 10a) was almost unmodified from the $s = 0.25$ case (not shown). With larger s , the laminar regime disappeared for values of Q larger than $6 \text{ cm}^3 \text{ s}^{-1}$. The transition to the eddy regime occurred for $1.3 \leq f \leq 1.8 \text{ s}^{-1}$ and for $1.8 \leq f \leq 2.0 \text{ s}^{-1}$, for $s = 0.4$ (Fig. 10b) and $s = 0.5$ (not shown), respectively.

A similar trend was observed while increasing the reduced gravity g' from 2 to 10 cm s^{-2} and keeping the slope constant at $s = 0.30$ (not shown). The wave regime was present for values of $Q \geq 2 \text{ cm}^3 \text{ s}^{-1}$ and $f \leq 0.6 \text{ s}^{-1}$ for $g' = 4 \text{ cm s}^{-2}$ and for almost all values of Q for $f \leq 1.2 \text{ s}^{-1}$ and $g' = 10 \text{ cm s}^{-2}$. Again, the laminar regime disappeared for the highest values of Q , and for $g' = 10 \text{ cm s}^{-2}$ it was only present for $Q \leq 3 \text{ cm}^3 \text{ s}^{-1}$ and the transition to eddies occurred for f between 1.5 and 2.2 s^{-1} .

As expected, the eddies were present for the larger values of the Coriolis parameter. The wave regime was observed for larger values of f when increasing the bottom slope s or the reduced gravity g' . From (13) and (14) the velocities in the lower layer are directly proportional to $v_p = g's/f$; therefore, increasing f will decrease the velocity of the dense current, while increasing s or g' will increase its value.

In some cases, increasing the flow rate Q while the other parameters were kept constant (Fig. 10) caused the flow to be in a different regime. It was observed that increasing the value of Q caused an increase of the dense lower layer depth H . Hence, we expect a decrease of the Ekman number and an increase of the velocity U while increasing Q and keeping all other parameters fixed. The experiments in the laminar and wave regimes had a tendency to increase their Froude number with increasing Q , hence explaining the transition from laminar to wave regime observed. Also, the increase in H observed for increasing values of Q induced the column of freshwater above the dense current to reduce its initial height. Hence, it experienced a larger "stretching" while it was carried downslope and eddies formed for sufficiently large f , explaining the transition to the eddy regime observed while increasing Q for large values of f .

In order to determine whether the gravity wave speed $\sqrt{g'H \cos\theta}$ was the critical velocity required by the dense current to generate waves in the bottom dense layer, we computed the value of the Froude number for a dense current over a sloping bottom (Turner 1973), $Fr = U/\sqrt{g'H \cos\theta}$. Here, U is the magnitude of the average velocity in the lower dense layer [as defined later in (27)]. We had observed that two successive wave crests never merged while moving downslope, and that the wave velocity measured for different time intervals (section 3) was approximately the same. Hence we assumed that, for each experiment, all the waves had the same speed and that this speed was constant in time. Furthermore,

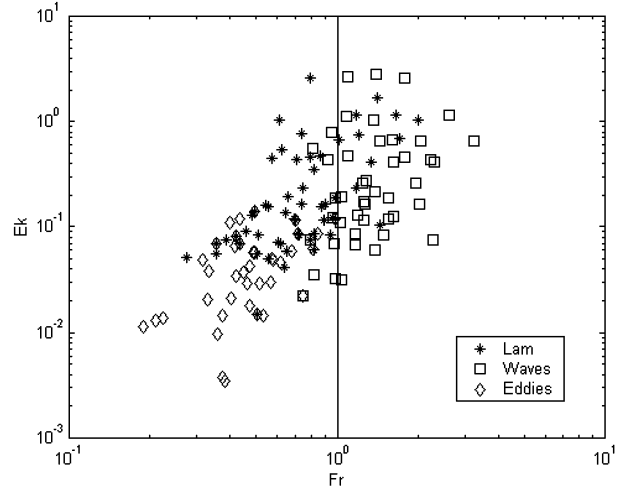


FIG. 11. Value of the Froude number $Fr = U/\sqrt{g'H \cos\theta}$, where $U = \sqrt{u_{2av}^2 + v_{2av}^2}$ vs values of the Ekman number $Ek = (\delta/H)^2$. The wave regime occurred primarily for values of $Fr \geq 1$, while the laminar and eddy regimes occurred for $Fr < 1$ and $Ek > 0.1$ and $Ek < 0.1$, respectively.

we assumed that in the wave regime the dense fluid forming the waves moved with the velocities u_2 and v_2 given by (13) and (14) (i.e., in the wave regime the entire transport is associated with the waves). As shown in Fig. 7, the perturbations to the mean flow in the wave regime were highly nonlinear and had such high amplitudes (a few mm) that the dense fluid in the current was redistributed in "blobs" corresponding to the wave crests, while in the wave troughs the thickness of the dense fluid decreased to less than a millimeter (almost a dry region), thinner than the Ekman layer thickness, which varied between $0.1 < \delta < 0.7 \text{ cm}$. Hence, we assumed that a wave of amplitude H moved downslope with a velocity U equal to the velocity of a dense layer of thickness H . The theoretical velocities obtained using this assumption have been compared with the measured velocities U_{exp} of the wave crests, giving good agreement (see Fig. 13). The magnitude of the velocity of a dense layer of depth H has been defined as

$$U = \sqrt{u_{2av}^2 + v_{2av}^2}, \quad (27)$$

where

$$u_{2av} = \frac{1}{H} \int_{-H}^0 u_2 dz \quad \text{and} \quad v_{2av} = \frac{1}{H} \int_{-H}^0 v_2 dz, \quad (28)$$

and it has been calculated for each experiment as well as the value of the Froude number and the Ekman number as shown in Fig. 11. From Figs. 11 and 12 it is clear that the wave regime occurred for $Fr \geq 1$. Assuming that the waves initially behaved as long waves, this indicates that the gravity wave speed was indeed the critical velocity required for the dense current in order for the waves to be produced. The error in evaluating the theoretical velocity U was mainly associated with the error in measuring the current depth H ; however,

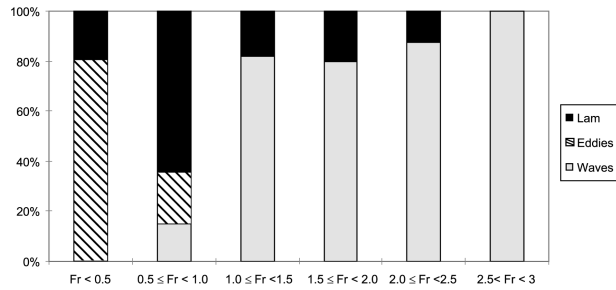


FIG. 12. Bar graph showing the percentages of experiments in the laminar (black), wave (light gray), and eddy (cross hatches) regimes for different Froude number bins.

the clear distinction between the laminar and wave regimes observed when increasing the Froude number above 1 gives us confidence that, despite having an error in evaluating U , we were still able to determine a critical Fr for the transition from the laminar to the wave regime. Once formed, the waves grew to large amplitude and became nonlinear and, at this later stage, the long-wave approximation is no longer valid. Both the wave and the laminar regimes occurred primarily for values of the $Ek > 0.1$ while the eddy regime occurred for $Ek < 0.1$. The Reynolds number did not show any correlation with the different regimes and ranged between $0 < Re < 300$.

The value of the experimental velocity U_{exp} of the dense current, defined as the velocity of the current head or of the wave crests, was measured for a representative number of the experiments in the laminar and wave regimes. We used the technique described in section 3 but, due to the time consuming aspects of the technique, did not analyze all of the experiments. The theoretical values of the velocity U of the current head (in the laminar regime) or of the wave crests (in the wave regime) were in good agreement with the measured experimental velocity U_{exp} for low values U , as shown in Fig. 13. The quality of the agreement decreased for increasing values of U , in which case it is possible that the steady state theoretical velocity U was not attained by the dense current within the finite length of the tank. It is possible that experiments on longer slopes would give better agreement for high values of U . We again computed the values of Froude and Ekman numbers using the measured experimental velocity U_{exp} , and, as shown in Fig. 14, the result was very similar to the result obtained with the theoretical velocity U (Fig. 11) with the wave regime occurring for approximately $Fr \geq 1$.

Furthermore, we measured the angle between the trajectory of the dense fluid and the horizontal. This angle decreased approximately linearly with increasing Coriolis parameter f , as expected. The values of the measured wavelength (obtained using the technique described in section 3) did not show any dependence on the parameters varied during the experiments and ranged, for the most part, from 4 to 6 cm.

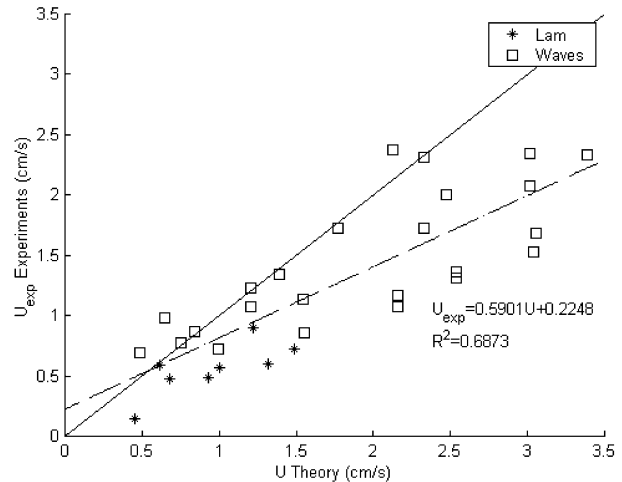


FIG. 13. Theoretical velocity $U = \sqrt{u_{2av}^2 + v_{2av}^2}$ vs the measured experimental velocity U_{exp} . The solid line is the 1:1 line. The dashed line is the linear regression of the data.

7. Mixing induced in the wave regime

The experiments described in this section were designed to study the mixing between the dense current and the overlying fresh ambient water. In particular, we wanted to quantify how efficient the waves were in mixing the two water masses. We believe that mixing between the dense salty water and the lighter freshwater was caused by breaking waves as shown in Fig. 8. For some parameter values the waves grew to such large amplitudes that they were observed to break in a three-dimensional fashion, possibly increasing the amount of mixing. As discussed in section 3, we measured the density of the dense current after it descended the slope

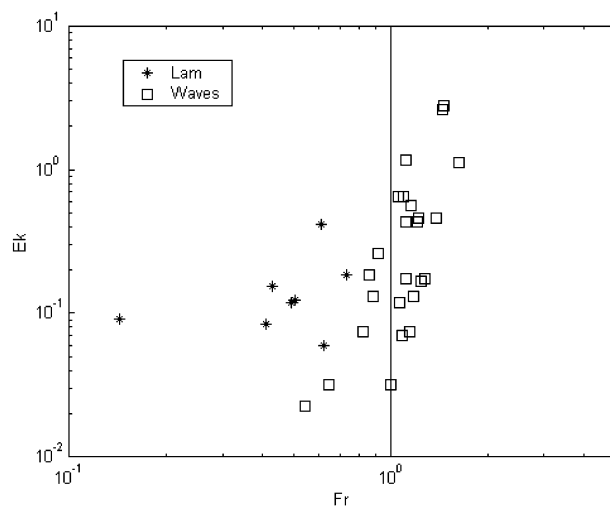


FIG. 14. Value of the Froude number $Fr = U_{exp}/\sqrt{g'H \cos\theta}$, where U_{exp} , defined as the velocity of the current head or of the wave crests, is the experimental velocity measured with the technique described in section 3 vs values of the Ekman number $Ek = (\delta/H)^2$. The wave regime occurred mainly for values of $Fr \geq 1$, while the laminar regime occurred for $Fr < 1$.

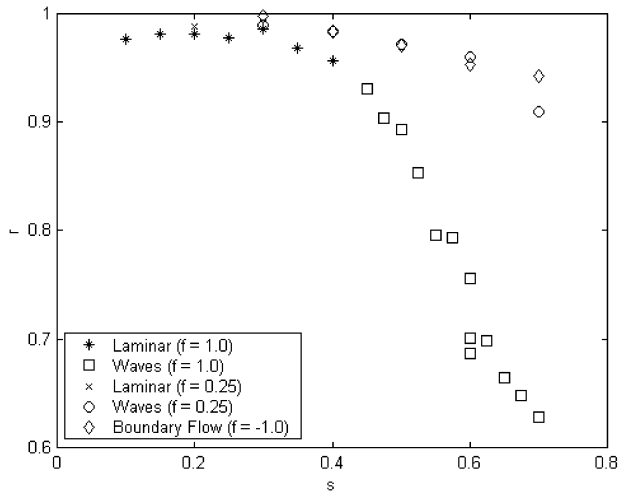


FIG. 15. Mixing ratio $r = (\rho_b - \rho_1)/(\rho_2 - \rho_1)$ dependence on the slope s ($Q = 2.5 \text{ cm}^3 \text{ s}^{-1}$ and $g' = 4 \text{ cm s}^{-2}$).

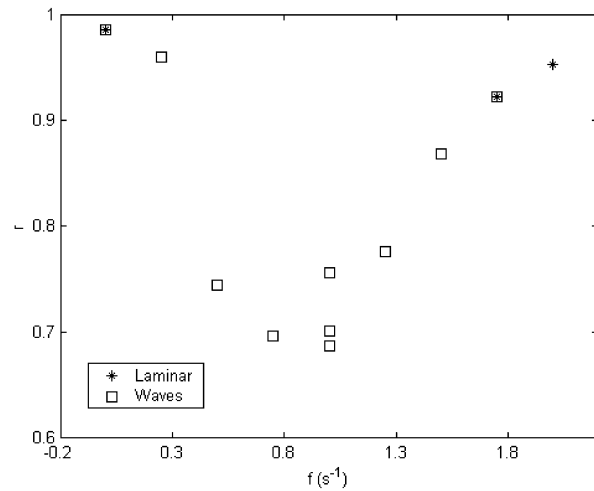


FIG. 16. Mixing ratio $r = (\rho_b - \rho_1)/(\rho_2 - \rho_1)$ dependence on the Coriolis parameter f ($Q = 2.5 \text{ cm}^3 \text{ s}^{-1}$, $s = 0.6$, and $g' = 4 \text{ cm s}^{-2}$).

(ρ_b) (see Fig. 4, insert i), and we quantified the amount of mixing by the mixing ratio $r = (\rho_b - \rho_1)/(\rho_2 - \rho_1)$, where $r = 1$ when there is no mixing and $r \rightarrow 0$ in the completely mixed case.

We first investigated the dependence of the mixing ratio on the slope angle for fixed values of the Coriolis parameter, reduced gravity, and flow rate. As shown in Fig. 15, the effect of the waves on the mixing was most evident for $f = 1.0 \text{ s}^{-1}$. For this value of the Coriolis parameter, the mixing ratio dramatically decreased when passing from the laminar to the wave regime. For s between 0.1 and 0.4, we observed a laminar regime with very little mixing occurring within the current. However, for $s > 0.4$ waves began to appear at the interface between the dense current and the freshwater above, and the mixing ratio decreased from 0.931, for $s = 0.45$, to 0.628, for $s = 0.70$. During those experiments, because of the high value of f , the dense current had a strong zonal velocity component and it encountered the left wall of the tank (when looking upslope) before reaching the bottom of the slope. After reaching the left wall, the dense current descended downslope along the wall until it reached the bottom pocket (see section 3; Fig. 4, insert i) where samples of dense water were collected. In order to investigate the possibility that the mixing was taking place at the boundary (left) wall and not on the slope where waves were observed, we conducted two different sets of experiments. First, we reduced the Coriolis parameter to $f = 0.25 \text{ s}^{-1}$. Hence, the zonal velocity component of the dense current diminished and the dense flow no longer encountered the left wall during its descent. Instead, it moved downslope until it reached the bottom pocket. The values of the mixing ratio r are shown in Fig. 15. Although r decreased from 0.990 to 0.909 after entering the wave regime at $s = 0.3$, the reduction was less significant than in the experiments with $f = 1.0 \text{ s}^{-1}$. Second, we

reversed the direction of rotation of the table, creating a clockwise rotation with a Coriolis parameter $f = -1.0 \text{ s}^{-1}$. The dense current had a zonal velocity in the opposite direction than for $f = 1.0 \text{ s}^{-1}$ and it encountered the right (looking upslope) wall soon after exiting the source. Hence, during the clockwise experiments, waves never appeared and all the mixing was observed during the descent along the boundary wall. The results shown in Fig. 15 indicate that some mixing occurred due to the boundary wall, with a reduction in the mixing ratio from 0.998 to 0.943 as the slope was increased from $s = 0.3$ to $s = 0.7$. However, the mixing observed during these experiments accounts for only 16%–27% of the total mixing measured for $f = 1.0 \text{ s}^{-1}$. Therefore, we were confident that the mixing along the boundaries is only a small contribution to the mixing generated by the waves.

We performed further experiments investigating the dependence of the mixing ratio on the Coriolis parameter f , varying f between 0 and 2 s^{-1} with the slope set to $s = 0.6$. The results shown in Fig. 16 suggest that the mixing ratio decreased while increasing f until it reached the minimum value for $f = 1 \text{ s}^{-1}$ and for values $f > 1 \text{ s}^{-1}$, it increased again. This behavior can be explained by examining the regimes for different values of f . For $f = 0 \text{ s}^{-1}$, the waves only appeared close to the bottom of the slope. Therefore the mixing produced by waves was active for a very short distance. For greater f , the waves were present over a larger portion of the slope and had a larger amplitude. After $f > 1$, the behavior reversed and the waves reduced in amplitude and appeared on a smaller portion of the slope until, for $f = 2 \text{ s}^{-1}$, the flow was laminar everywhere on the slope. Hence, this result ensured that the difference in mixing between the $f = 1 \text{ s}^{-1}$ and $f = 0.25 \text{ s}^{-1}$ sets of experiments was due to the difference in rotation rate and not due to the fact that, for $f = 1 \text{ s}^{-1}$, the currents

encountered the left (looking upslope) wall and more mixing occurred because of the wall.

We conducted a few experiments investigating the effect of a nonuniform sloping bottom by adding some across-slope topographic perturbations. The perturbations were obtained by placing some tubing of diameter 8 mm across slope, following an isobath, so that the perturbation depth was higher than the dense current thickness (a few millimeters) and the bottom boundary layer depth ($\delta = 1.4$ mm). Experiments were performed with one, two, and three topographic perturbations on the slope. The differences of the mixing ratio r between the three experiments were negligible and were approximately the same values found with a sloping bottom with no perturbations. Hence, these experimental results suggested that small perturbations to the bottom topography were not responsible for enhancing the mixing between the bottom dense current and the ambient water.

8. Discussion and conclusions

Density-driven currents in a two-layer rotating system over a sloping bottom were produced in a laboratory tank. Dense fluid, supplied continuously through a nozzle on the right side (looking upslope) of the shallowest part of the tank, started flowing downslope turning right (looking downstream) influenced by the Coriolis force and increasing its width while descending the slope. Four parameters were varied in different experiments: the Coriolis parameter f , the reduced gravity g' , the slope angle s , and the flow rate Q . Over a wide range of parameters, the following three flow types were observed: the laminar regime, in which the dense current had constant thickness behind the nose; the wave regime, in which a locally planar wave disturbance appeared on the interface between the dense and fresh fluids as shown in Figs. 6 and 7; and the eddy regime, in which periodic formation of cyclonic eddies in the overlying fresh ambient fluid was observed. All of the experiments revealed that, for increasing slope angle and reduced gravity, the transition between the laminar and the wave regime occurred at higher values of f . Furthermore, increasing the rotation frequency induced the formation of the eddies.

A linear steady theory including viscous effects and rotation has been developed for a rotating dense current over a sloping bottom. For large values of the Ekman number, the velocity of the dense current had the form of a simple viscous flow down a slope. The fluid had a single Ekman layer adjacent to the sloping bottom. For small values of the Ekman number, the flow had three Ekman layers (Fig. 2). One was next to the sloping bottom and the other two were above and below the interface between the dense and fresh fluid. The theoretical velocity of the dense current obtained with this model agreed with the speed of the dense fluid in the laminar and wave regimes, provided the theoretical ve-

locity was not too high. Large values of the theoretical velocity provided an upper bound to the speed of the dense fluid in the wave regime.

Both the theoretical and measured values of the velocity gave values of the Froude number less than unity for the experiments in the laminar regime, while the wave regime was observed for values of the Froude number larger or approximately equal to unity. This behavior suggests that wave generation requires that the current speed reach or overcome a critical velocity given by the gravity wave speed $\sqrt{g'H \cos\theta}$. We believe the observed waves are a manifestation of the roll wave instability (Baines 1995) in the bottom dense layer. Roll waves are the spatially periodic steady solutions of the equations of motion for nonrotational downslope flows with frictional drag for $Fr_D > 2$, where Fr_D is the Froude number defined using the steady equilibrium solution obtained with a frictional drag represented by a quadratic drag law

$$U_D = \sqrt{\frac{g'H \sin\theta}{C_D}} \quad (29)$$

and C_D is the drag coefficient. If we assume that the term associated with the frictional drag $-C_D(U_D^2/H)$ is substituted by the viscous term in Eq. (3), $\nu(\partial^2 u_2/\partial z^2)$ scaled as $\nu(U_D/H^2)$, we obtain $C_D = \nu/HU_D = 1/Re$. This definition of the drag coefficient is found to be a good approximation at low Reynolds numbers (Tritton 1988), appropriate to our experiments. Substituting C_D into Eq. (29) gives a value for the velocity $U_D = 2v_v$, where v_v is the Stokes flow velocity defined in section (2b) for a nonrotating layer of viscous fluid traveling down the slope. Hence we would expect roll waves to appear for values of the Froude number $Fr_v > 1$ when defined using the Stokes flow velocity. The Stokes flow is the solution of the equations of motion (1)–(4) in the limit of $f = 0$ (i.e., large Ek; see section 2b). The wave regime observed for the nonrotating experiments qualitatively presented no differences with the wave regime observed in the rotating experiments. Hence, assuming the mechanism for roll wave formation is not drastically affected by rotation, we would expect roll waves to appear for $Fr > 1$, as observed in our experiments when Fr is defined using the velocity of the rotating viscous flow given by (27). We discard the possibility that the observed waves are an expression of the Ekman layer instability since the Rossby and Reynolds numbers do not collapse on the stability curves given by Tatro and Mollo-Christensen (1967). Furthermore the Richardson number for the majority of the wave regime experiments was larger than 1/4, with only seven experiments having a Richardson number less than 1/4 hence, we believe that the waves that we observed are not an expression of the Kelvin–Helmholtz instability.

The auto- and cross-correlation technique (see section 3) were viable tools for measuring the length and speed of the waves. For the first time, both across- and

downslope components of the velocity have been measured for a dense current down a slope in a rotating environment. (In the present paper we presented only the total velocity obtained as a sum of the two components mentioned above.) This allows for a more accurate estimate of the Froude number when compared to previous experiments that measured only the downslope component of the velocity (Shapiro and Zatsepin 1996; Zatssepin et al. 1996). As discussed above, in the present experiments the roll waves manifested for $Fr > 1$, while in Shapiro and Zatssepin (1996) and Zatssepin et al. (1996) waves appeared for values of $Fr > 0.6$, where the Froude number was based on the downslope velocity of the front, neglecting the azimuthal component of the velocity. A “wavy-eddy” regime was also observed by Nagata et al. (1993) and this flow pattern was determined by two nondimensional parameters: the nondimensional density difference $\rho^* = g'/f^2 H$ and the Taylor number $Ta = f^2 H^4/\nu^2$. The values of these nondimensional parameters for the experiments discussed in the present paper span a much larger range and do not show any consistent pattern when compared to the flow regime diagram of Nagata et al. (1993) constructed with only 10 experiments. The dense current generation employed in Nagata et al. (1993) was different than in the present study and, given the limited number of experiments, it is difficult to understand why the Nagata et al. (1993) results collapse for different nondimensional numbers than in the present study. The eddy regime was qualitatively similar to Lane-Serff and Baines (1998, 2000) and Etling et al. (2000); however, the values of the nondimensional parameters indicating the importance of the viscous draining and relative stretching used by Lane-Serff and Baines (1998) for which eddies were observed were slightly different. In the present study, eddies were observed for values of the viscous draining parameter larger than 9 instead of 3.5, and values of the relative stretching larger than 0.02 instead of 0.07. The nature of the present experiment is different than Lane-Serff and Baines (1998) since it presents lower flow rates and density differences, steeper slopes, and slightly lower Coriolis parameters. The focus of the present work was the wave regime and not the eddy regime, hence we did not investigate any further a possible explanation for the slightly different values of those nondimensional parameters for which we found eddies when compared with Lane-Serff and Baines (1998).

Furthermore, we investigated the mixing between the dense fluid and the fresh overlying fluid in both laminar and wave regimes. Mixing was enhanced when passing from the laminar to the wave regime and it also increased with increasing the Froude number. The highest values of mixing occurred for a value of the Coriolis parameter $f = 1 \text{ s}^{-1}$.

Since one objective of this study is to understand mixing by such density currents, we conducted the fol-

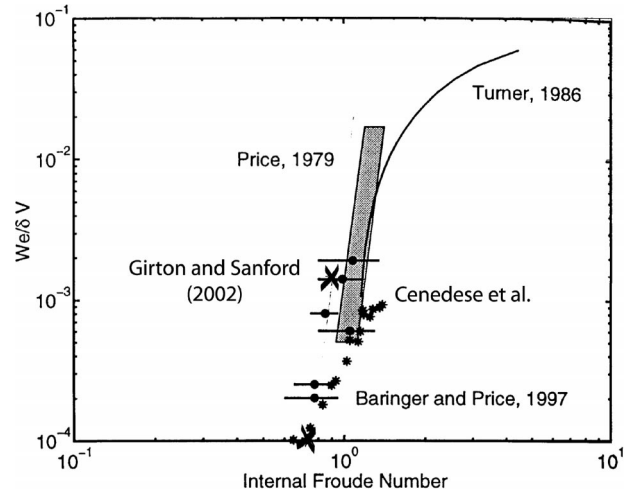


FIG. 17. Entrainment rate W_e , normalized by the velocity difference $\delta V (= U_{exp})$, plotted against the internal Froude number. Data are from laboratory experiments analyzed by Price (1979) (shaded area) and Turner (1986) (solid line) and from estimates of the Mediterranean outflow by Baringer and Price (1997) (solid dots) and of the Denmark Strait overflow by Girton and Sanford (2002) (crosses) and for the present experiments (stars). Readapted from Price and Yang (1998).

lowing analysis of the data. From the values of the mixing ratio, r , obtained in the laboratory, we estimated the value of the entrainment rate

$$W_e = \frac{1}{A} Q \left(\frac{1}{r} - 1 \right),$$

defined as the averaged vertical velocity at the interface necessary to obtain the observed mixing between the dense fluid and the fresh overlying fluid over an area A . (We estimated the area A covered by the dense flow to be approximately one-half of the sloping bottom area and equal to $A = 1090.5 \text{ cm}^2$.) In order to normalize W_e with the fluid velocity, we wanted to measure the experimental velocity U_{exp} for the experiments for which mixing was measured. However, the experimental setup and poor quality of the imaging prevents measurement of the current velocity from the experiments as described in section 3. Therefore, we used the data in Fig. 13 to find a relationship between the theoretical velocity U and U_{exp} . A linear regression of the data gives the expression $U_{exp} = 0.5901U + 0.2248$, with an $R^2 = 0.6873$. The use of a linear regression is meant to account for the discrepancy between U and U_{exp} at large values of U as discussed in section 6. Hence, we normalized W_e by the estimated experimental velocity U_{exp} given by the expression above and calculated the Froude number using this U_{exp} .

These results are shown in Fig. 17 and are compared with previous laboratory and observational values investigated by Price and Yang (1998) and some new observational values (Girton and Sanford 2003). Figure 17 shows that the present laboratory results (stars) had a somewhat lower normalized entrainment rate than the

experiments analyzed by Price (1979) and Turner (1986), which presented classical turbulent entrainment behavior. However, these values were comparable to the estimates of the Mediterranean overflow (solid dots) (Baringer and Price 1997a,b) and to the Denmark Strait overflow (crosses) (Girton and Sanford 2002). The agreement between the observations and the laboratory experiments was encouraging and indicated that the waves observed in the present experiments may be a possible candidate for the mixing observed during oceanic overflows.

Acknowledgments. We thank Jason Hyatt, Paul Linden, and Jim Price for providing invaluable discussions, carefully reading drafts, and substantially improving the clarity of the manuscript. Support was given by the Office of Naval Research Office of Polar Programs under Grant N00014-99-1-0366, and the National Science Foundation under Grant OCE-0095427. The laboratory experiments were carried out with the able assistance of John Salzig and Keith Bradley.

REFERENCES

- Aagaard, K., L. K. Coachman, and E. C. Carmack, 1981: On the halocline of the Arctic Ocean. *Deep-Sea Res.*, **28**, 529–545.
- Alavian, V., and A. M. Asce, 1986: Behavior of density currents on an incline. *J. Hydrol. Eng.*, **112**, 27–42.
- Baines, P. G., 1995: *Topographic Effects in Stratified Flows*. Cambridge University Press, 482 pp.
- , and S. Condie, 1998: Observations and modeling of Antarctic downslope flows: A review. *Ocean, Ice and Atmosphere: Interactions at the Antarctic Continental Margin*, S. Jacobs and R. Weiss, Eds., Amer. Geophys. Union, 29–49.
- Baringer, M. O., and J. F. Price, 1997a: Mixing and spreading of the Mediterranean outflow. *J. Phys. Oceanogr.*, **27**, 1654–1677.
- , and —, 1997b: Momentum and energy balance of the Mediterranean outflow. *J. Phys. Oceanogr.*, **27**, 1678–1692.
- Britter, R. E., and P. F. Linden, 1980: The motion of the front of a gravity current travelling down an incline. *J. Fluid Mech.*, **99**, 531–543.
- Bruce, J. G., 1995: Eddies southwest of the Denmark Strait. *Deep-Sea Res.*, **42**, 13–29.
- Chapman, D. C., and G. Gawarkiewicz, 1995: Offshore transport of dense shelf water in the presence of a submarine canyon. *J. Geophys. Res.*, **100**, 13 373–13 387.
- Davies, P. A., Y. Guo, and E. Rotenberg, 2002: Laboratory model studies of Mediterranean outflow adjustment in the Gulf of Cadiz. *Deep-Sea Res.*, **49**, 4207–4223.
- Dickson, R. R., and J. Brown, 1994: The production of North Atlantic deep water: Sources, rates and pathways. *J. Geophys. Res.*, **99**, 12 319–12 341.
- Ellison, T. H., and J. S. Turner, 1959: Turbulent entrainment in stratified flows. *J. Fluid Mech.*, **6**, 423–448.
- Etling, D., F. Gelhardt, U. Schrader, F. Brennecke, G. Kuhn, G. Chabert d'Hieres, and H. Didelle, 2000: Experiments with density currents on a sloping bottom on a rotating fluid. *Dyn. Atmos. Oceans*, **31**, 139–164.
- Foster, T. D., and E. C. Carmack, 1976: Frontal zone mixing and Antarctic Bottom Water formation in the southern Weddell Sea. *Deep-Sea Res.*, **23**, 301–317.
- Girton, J. B., and T. B. Sanford, 2003: Descent and modification of the overflow plume in Denmark Strait. *J. Phys. Oceanogr.*, **33**, 1351–1364.
- Griffiths, R. W., 1986: Gravity currents in rotating systems. *Annu. Rev. Fluid Mech.*, **18**, 59–89.
- Jiang, L., and W. J. Garwood, 1995: A numerical study of three-dimensional bottom plumes on a Southern Ocean continental slope. *J. Geophys. Res.*, **100**, 18 471–18 488.
- , and —, 1996: Three-dimensional simulations of overflows on continental slopes. *J. Phys. Oceanogr.*, **26**, 1224–1233.
- , and —, 1998: Effects of topographic steering and ambient stratification on overflows on continental slopes: A model study. *J. Geophys. Res.*, **103**, 5459–5476.
- Jungclauss, J. H., and J. O. Backhaus, 1994: Application of a transient reduced gravity plume model to the Denmark Strait overflow. *J. Geophys. Res.*, **99**, 12 375–12 396.
- Killworth, P. D., 1977: Mixing on the Weddell Sea continental slope. *Deep-Sea Res.*, **24**, 427–448.
- Krauss, W., 1996: A note on overflow eddies. *Deep-Sea Res.*, **43**, 1661–1667.
- Lane-Serff, G. F., and P. G. Baines, 1998: Eddy formation by dense flows on slopes in a rotating fluid. *J. Fluid Mech.*, **363**, 229–252.
- , and —, 2000: Eddy formation by overflows in stratified water. *J. Phys. Oceanogr.*, **30**, 327–337.
- Morel, Y., and J. McWilliams, 2001: Effects of isopycnal and diapycnal mixing on the stability of oceanic currents. *J. Phys. Oceanogr.*, **31**, 2280–2296.
- Mory, M., M. E. Stern, and R. W. Griffiths, 1987: Coherent baroclinic eddies on a sloping bottom. *J. Fluid Mech.*, **183**, 45–62.
- Nagata, Y., R. Kimura, H. Honji, Y. Yamazaki, K. Kawaguchi, and T. Hosoyamada, 1993: Laboratory experiments of dense water descending a continental slope. *Deep Ocean Circulation: Physical and Chemical Aspects*, T. Teramoto, Ed., Elsevier Science, 333–350.
- Nof, D., 1983: The translation of isolated cold eddies on a sloping bottom. *Deep-Sea Res.*, **30**, 171–182.
- Özgökmen, T. M., and E. P. Chassignet, 2002: Dynamics of two-dimensional bottom gravity currents. *J. Phys. Oceanogr.*, **32**, 1460–1478.
- Price, J. F., 1979: On the scaling of stress-driven entrainment experiments. *J. Fluid Mech.*, **90**, 509–529.
- , and M. O. Baringer, 1994: Outflows and deep water production by marginal seas. *Progress in Oceanography*, Vol. 33, Pergamon, 161–200.
- , and J. Yang, 1998: Marginal sea overflows for climate simulations. *Ocean Modeling and Parametrization*, E. Chassignet and J. Verron, Eds., Kluwer Academic, 155–170.
- , and Coauthors, 1993: Mediterranean outflow mixing and dynamics. *Science*, **259**, 1277–1282.
- Saunders, P. M., 1990: Cold outflow from the Faroe Bank Channel. *J. Phys. Oceanogr.*, **20**, 29–43.
- Schmidt, W., 1911: Zur mechanik der boen. *Z. Meteor.*, **28**, 355–362.
- Schubert, G., and D. L. Turcotte, 2002: *Geodynamics*. 2d ed. Cambridge University Press, 456 pp.
- Shapiro, G. I., and A. G. Zatsepin, 1996: Gravity current down a steeply inclined slope in a rotating fluid. *Ann. Geophys.*, **15**, 366–374.
- , and A. E. Hill, 1997: Dynamics of dense water cascade at the shelf edge. *J. Phys. Oceanogr.*, **27**, 2381–2394.
- Simpson, J. E., 1997: The anatomy of a gravity current. *Gravity Currents in the Environment and the Laboratory*. 2d ed., Cambridge University Press, 140–163.
- Smith, P. C., 1975: A streamtube model for bottom boundary currents in the ocean. *Deep-Sea Res.*, **22**, 853–873.
- , 1977: Experiments with viscous source flows in rotating systems. *Dyn. Atmos. Oceans*, **1**, 241–272.
- Spall, M. A., and J. F. Price, 1998: Mesoscale variability in Denmark Strait: The PV outflow hypothesis. *J. Phys. Oceanogr.*, **28**, 1598–1623.
- Swaters, G. E., 1998: Numerical simulation of the baroclinic dynamics of density-driven coupled fronts and eddies on a sloping bottom. *J. Geophys. Res.*, **103**, 2945–2962.

- Tatro, P. R., and E. L. Mollo-Christensen, 1967: Experiments on Ekman layer instability. *J. Fluid Mech.*, **28**, 531–544.
- Tritton, D. J., 1988: *Physical Fluid Dynamics*. Clarendon Press, 519 pp.
- Turner, J. S., 1973: Buoyant convection from isolated sources. *Buoyancy Effects in Fluids*, Cambridge University Press, 165–206.
- , 1986: Turbulent entrainment: The development of the entrainment assumption and its application to geophysical flows. *J. Fluid Mech.*, **170**, 431–471.
- Warren, B. A., 1981: Deep circulation of the World Ocean. *Evolution of Physical Oceanography, Scientific Surveys in Honor of Henry Stommel*, B. A. Warren and C. Wunsch, Eds., The MIT Press, 6–41.
- Whitehead, J. A., 1998: Topographic control of oceanic flows in deep passages and straits. *Rev. Geophys.*, **36**, 423–440.
- , M. Stern, G. Flierl, and B. Klinger, 1990: Experimental observations of baroclinic eddies on a sloping bottom. *J. Geophys. Res.*, **95**, 9585–9610.
- Zatsepin, A. G., A. G. Kostyanoi, and A. V. Semenov, 1996: An axisymmetric density current over a sloping bottom in a rotating fluid. *Oceanology*, **36**, 311–316.